THE JOURNAL OF PHYSICAL CHEMISTRY C
A JOURNAL OF THE AMERICAN CHEMICAL SOCIETY

pubs.acs.org/JPCC

Article

On the Utility of Ce^{3+} Spin–Orbit Transitions in the Interpretation of Rate Data in Ceria Catalysis: Theory, Validation, and Application

Sadia Afrin and Praveen Bollini*

Cite This: *J. Phys. Chem. C* 2023, 127, 234–247

Read Online

ACCESS | Metrics & More | Article Recommendations | Supporting Information

ABSTRACT: Cerium oxide is a ubiquitous component in catalytic systems of industrial and academic interest, and the precise mechanistic function of oxygen vacancies/Ce^{3+} ions a persistent open question in this regard. Existing methods for quantifying vacancy densities are for the most part indirect in nature, and they either have to necessarily be applied ex situ or, if applicable in situ, are oftentimes limited in applicability or quantitative rigor. We present herein a theoretical and experimental analysis of the utility of $^2F_{5/2}$–$^2F_{7/2}$ electronic transitions in the quantitative estimation of oxygen vacancy or Ce^{3+} densities. Application of crystal field theory reveals the nonforbidden nature of $^2F_{5/2}$–$^2F_{7/2}$ transitions for Ce^{3+} ions present in a C_{3v} site symmetry environment, unlike free Ce^{3+} ions in the gas phase that exhibit La Porte forbidden transitions between states of equivalent parity. The molar extinction coefficient for the infrared feature of interest is estimated using three reductants—H_2, CO, and ethanol—and applied toward interpretation of ceria-catalyzed H_2–D_2 exchange and *tert*-butanol dehydration catalysis rate data. Linear correlations between H_2–D_2 exchange rates and infrared spectroscopy-derived vacancy densities point to the sole involvement of reduced domains in H_2 activation steps prevalent in hydrogenation and hydrodeoxygenation catalysis. Contrastingly, areal *tert*-butanol dehydration rates that trend inversely with vacancy densities both in the presence and absence of α-hydrogen-containing oxygenates carrying a propensity toward stoichiometric oxidative routes suggest the participation of oxidized, not reduced domains in dehydrative turnovers producing isobutene. The nonforbidden nature of the $Ce^{3+2}F_{5/2}$–$^2F_{7/2}$ transition—evidenced here using symmetry considerations—likely extends beyond the C_{3v} symmetry environment under consideration here, implying that its fortuitous appearance within the infrared region of the electromagnetic spectrum may render it amenable to quantitative application in relating local structure to catalytic function in ceria catalysis more broadly.

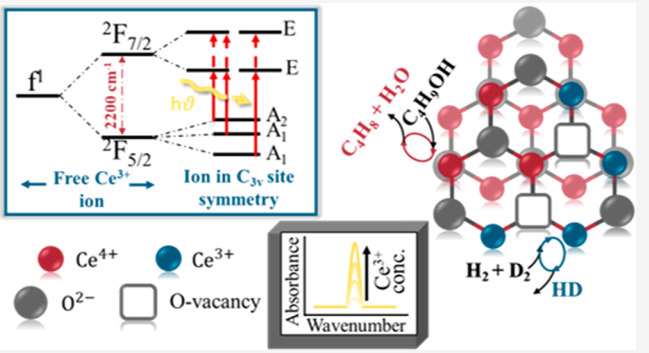

1. INTRODUCTION

Cerium oxide—the most abundant rare-earth oxide in the earth's crust[1]—is a common component in catalytic applications, examples of which include its use as an oxygen storage material in automotive exhaust emissions catalysis,[2−6] as a catalyst for water splitting[7] and water–gas shift reactions,[8−12] as an electrolyte in solid oxide fuel cells and oxygen membranes,[13,14] and as a catalyst support or promoter for a broad range of organic transformations.[3,4,15] Especially important is its use in expanding the operating window for three-way catalysts[2,13]—an application enabled by its propensity to act as a reversible oxygen sponge through the creation and healing of oxygen vacancies during rich and lean cycles, respectively.[15−17]

A recurring theme in ceria catalysis research pertains to the effect of surface reduction/oxygen vacancy creation on catalytic function, with vacancies formed during redox cycles being proposed as active centers for oxygenate/hydrogen activation in alkanol dehydrogenation, aromatic oxygenate hydrodeoxygenation, and alkyne selective hydrogenation.[5,6,15,18−21] Theoretical as well as experimental studies have been used to claim that oxygenates such as aliphatic alcohols, phenols, and aldehydes exhibit improved interaction with reduced ceria surfaces compared to oxidized ones. Ferrizz et al. used temperature-programmed desorption to report an order of magnitude higher methanol dehydrogenation yields over reduced single-crystal ceria samples compared to stoichiometric ones—[22] an observation not unrelated to reports of increased methanol adsorption and a monotonic shift in the methoxy C–O vibrational frequency over polycrystalline ceria upon surface reduction.[20] Temperature-programmed surface reaction (TPSR) experiments and density

Received: September 16, 2022
Revised: November 20, 2022
Published: December 23, 2022

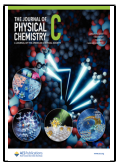

https://doi.org/10.1021/acs.jpcc.2c06637
J. Phys. Chem. C 2023, 127, 234–247

functional theory (DFT) calculations have been employed by Zhao et al.[23] and Calaza et al.[24] to suggest vacancy-mediated enolization of aldehydes. Schimming et al. noted a linear correlation between guaiacol conversion and oxygen vacancy density over ceria−zirconia materials, consistent with oxygen vacancies being the active center for guaiacol hydrodeoxygenation.[18] Branda and co-workers[25] reported improved interaction of H_2 with ceria surfaces in the presence of oxygen vacancies, consistent with correlations between H_2-D_2 exchange conversion and vacancy density presented by the Sievers group.[15] An abundance of suggestions as to the role of surface reduction/oxygen vacancy formation in acid catalysis also exist in the open literature. Binet et al., for example,[20] noted a decrease in acid strength of Ce cations upon surface reduction, and Overbury and co-workers rationalized the dependency of the strength and density of basic sites on nanoceria shape in terms of the variation in extent of coordinative unsaturation of cerium and oxygen atoms due to differing concentration of and propensities for formation of oxygen vacancies as a function of surface termination.[26] Our own previous work reveals the genesis of nonoxidative ethanol dehydrogenation catalytic function on ceria surfaces by means of its in situ reduction under anaerobic conditions,[6] reemphasizing the need for accurate characterization of Ce^{3+} ions/vacancy densities, preferably in situ, in order to more thoroughly elucidate structure−function relationships in ceria catalysis.

Techniques employed in the open literature to assess vacancy density include O_2 adsorption[15,18] and pulse[2] experiments, H_2/CO temperature-programmed reduction (TPR),[3,27,28] thermogravimetric analysis (TGA),[21] and spectroscopic techniques including X-ray photoelectron (XPS),[29−31] Raman,[31−35] UV−vis,[31] and Fourier transform infrared spectroscopy.[36,37] Many of the aforementioned methods for estimating vacancy density are highly indirect; examples include the tracking of TGA weight loss or gain, respectively, due to reduction by H_2/CO during TPR or reoxidation by O_2 during O_2 pulse experiments, the use of a mass spectrometer to measure reduction products (H_2O/CO_2) during ceria reduction,[6,38] and Raman and FTIR spectroscopy to track peroxide and superoxide formation upon O_2 adsorption.[36,37,39,40] Application of these indirect methods are typically conducted ex situ and may oftentimes provide vacancy density values that differ from those prevalent under reaction conditions. Techniques that can be applied in situ, rather than ex situ, on the other hand, also appear to have specific limitations of their own. The rigorous application of Raman spectroscopy toward estimating oxygen vacancy densities, for instance, is limited somewhat by the sensitivity of the CeO_2 fluorite phase I_D/I_{F2g} mode ratio to changes in reduction temperature and particle size.[31,33] Rigorous quantification of Ce^{3+} formation concurrent with vacancy creation using XPS, on the other hand, is rendered challenging due to the complex nature of overlapping Ce^{3+} and Ce^{4+} electron bands that require rigorous deconvolution of measured XPS spectra. These measurements also typically require ultrahigh vacuum conditions that restrict application of XPS under reaction conditions. It is evident that the availability of a characterization technique yielding accurate values of vacancy densities that are measured in situ would aid significantly in achieving a rigorous understanding of the relationship between oxygen understoichiometry and catalytic function—a theme that constitutes one of the more persistent open questions in the practice of ceria catalysis.

Noteworthy as regards the need for a more practicable in situ technique for characterizing Ce^{3+} densities is the appearance of a well-defined band near 2150 cm^{-1} that has now been identified in multiple studies reporting ceria infrared data;[15,41] despite its potential utility, application of this technique toward quantifying vacancy densities under reaction conditions remains relatively unexplored. We attempt in our study to address this gap in understanding of the basis for detection in the infrared region of the electromagnetic spectrum and demonstrate its use in the quantitative interpretation of catalytic rate data. Specifically, we present an application of principles of crystal field and group theory to establish the basis for the nonforbidden nature of $Ce^{3+2}F_{5/2}-{}^2F_{7/2}$ electronic transitions that appear at 2150 cm^{-1}, and demonstrate its use in testing hypotheses as to the role of oxidized/reduced ceria domains in redox and acid-catalyzed turnovers. Integrated molar extinction coefficients (E/cm·μmol^{-1}) estimated using three distinct reductants are used to track the densities of and to explain the mechanistic function of oxygen vacancies in H_2-D_2 exchange and *tert*-butanol dehydration catalysis. Methods and examples presented point to the utility of a quantitative analysis of this electronic transition toward addressing open questions in ceria catalysis.

2. EXPERIMENTAL SECTION

2.1. Catalyst Synthesis. Bulk cerium oxide was prepared using the procedure reported by Schimming et al.[18] Precipitation of cerium oxide was achieved by adding cerium(III) nitrate hexahydrate (Acros Organics TM, 99.5%) to an aqueous solution of ammonium hydroxide (ACS reagent grade, 28−30%). Specifically, a 0.1 M solution was prepared by dissolving 21.77 g of $Ce(NO_3)_3{\cdot}6H_2O$ in 498.6 g of deionized water. This solution was then added dropwise to 512 mL of aqueous NH_4OH (ACS reagent grade, 28−30%) with continuous stirring at a rate of 500 rpm over the course of 1.2 ks. The resulting precipitate was filtered using a hand vacuum pump and rinsed twice with 50 mL of deionized water for every 200 mL of solution filtered. The obtained powder was subsequently dried overnight at 373 K in an oven and calcined in a muffle furnace for 14.4 ks at 773 K under 3.33 $cm^3\ s^{-1}$ air (Matheson, zero-grade) with a ramp rate of 0.083 K s^{-1}—a procedure similar to prior literature reports.[42,43] Here 8.4 g of catalyst was recovered in the process of applying this synthesis protocol and used for further characterization and reactivity experiments.

2.2. Material Characterization. Powder X-ray diffraction patterns were collected on a Rigaku SmartLab Diffractometer using Cu Kα radiation (40 kV, 30 mA) in a 2θ range of 20−80° with a step size of 0.02° and scan rate of 0.167° s^{-1}. N_2 physisorption isotherms were measured using a Micromeritics 3 Flex instrument at 77 K, with samples degassed at 473 K and 10.67−13.33 Pa for 14.4 ks.

2.3. Surface Reduction Protocols. Ceria reduction experiments were performed in a Harrick high-temperature cell with BaF_2 windows (32 mm × 3 mm). Self-supporting wafers comprised of 40 mg of CeO_2 diluted with 25 mg of CaF_2 were heated to 773 K at a ramp rate of 0.167 K s^{-1} and then pretreated under a 5 kPa O_2 in a He flow of 0.35 $cm^3\ s^{-1}$ for 3.6 ks. The IR cell was then cooled to the temperature at which background spectra were collected—573 K for H_2, 473

https://doi.org/10.1021/acs.jpcc.2c06637
J. Phys. Chem. C 2023, 127, 234−247

Scheme 1. Splitting of the f^1 Configuration of Free Ce^{3+} Ions in the Gas Phase and Those Present in a C_{3v} Site Symmetry Environment into Nondegenerate States by Spin−Orbit Coupling and Crystalline Electrostatic Field Effects

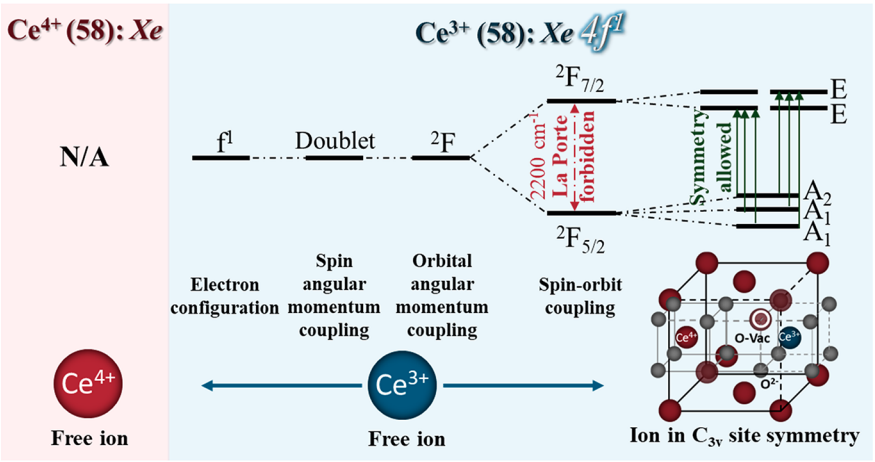

K for CO, and 373 K for ethanol—at a ramp rate of 0.167 K s^{-1} under N_2. Background spectra were collected at 573 K under N_2 flow, 473 K under CO flow, and 373 K under N_2 flow for ceria reduction with H_2, CO, and ethanol, respectively. The sample was then heated to the specific reduction temperature of interest followed by subjection to isothermal reduction steps performed at ambient pressure by flowing 13 kPa H_2/13 kPa CO/5.5 kPa ethanol, balance N_2. IR spectra were collected after 1.8 ks of isothermal reduction, and oxidation products (H_2O, CO_2) were quantified using an MKS Cirrus 3.0 mass spectrometer. Infrared spectra were collected using a Nicolet 6700 Fourier transform infrared (FTIR) spectrometer equipped with a deuterated triglycine sulfate (DTGS) detector averaging 64 scans at a resolution of 4 cm^{-1} and analyzed using the vendor-provided OMNIC software. All reported IR spectra were background subtracted.

2.4. Reactivity Studies. *2.4.1. H_2−D_2 Exchange.* H_2−D_2 exchange experiments were conducted using the FTIR setup described above. 65 mg self-supporting wafers (40 mg CeO_2 diluted with 25 mg CaF_2) were heated to 773 K at a ramp rate of 0.167 K s^{-1} and then pretreated under a 5 kPa O_2 in He flow of 0.35 cm^3 s^{-1} for 3.6 ks. When required, a prereduction step was conducted (after pretreatment) at the desired temperature under 7 kPa H_2 (Matheson, UHP), 20 kPa argon (Matheson, UHP grade, internal standard), and balance N_2. Water formation during the prereduction step was measured using an MKS Cirrus 3.0 mass spectrometer. The sample was then cooled to reaction temperature (373 K) at 0.167 K s^{-1} under N_2 for reaction over oxidized ceria or H_2 in N_2 for reaction over reduced ceria. Background spectra were collected under a flow of 9 kPa H_2, 13.2 kPa Ar, and balance N_2 at ambient pressure. Isotopic exchange reactions were performed by introducing equimolar (9 kPa) D_2 into the IR cell feedstream, following which absorbance spectra were collected at different time on stream values along with the continuous tracking of reactant and product molar flow rates using online mass spectrometry.

2.4.2. tert-Butanol Dehydration. Twenty-five mg of catalyst was loaded into a quartz tube (0.004 m inner diameter) mounted into an insulated single-zone furnace (1060 W/115 V, Applied Test Systems Series 3210) with a thermocouple (Omega, Model KMQXL-062U-15) placed at the top of the catalyst bed connected to an Applied Test Systems temperature controller (Model 17−16907) used to control bed temperature and ramp rates. The sample was heated to 773 K at a ramp rate of 0.046 K s^{-1} and then pretreated under a 5 kPa O_2 in He flow of 0.35 cm^3 s^{-1} for 3.6 ks. The sample was subsequently cooled to reaction temperature (433 K) under air at 0.021 K s^{-1}. Vapor phase alkanol dehydration was carried out by feeding a mixture containing *tert*-butanol, ethane (2.01% in He, Matheson, UHP grade, internal standard), and He. *tert*-Butanol (Sigma, 99%, ReagentPlus) or a mixture of *tert*-butanol and ethanol (Sigma, 99%, ReagentPlus) was fed to the reactor setup using a syringe pump (KD Scientific, model 100), with tubing downstream of the syringe pump heated to 373−393 K to prevent condensation of reactants and products. Spent catalysts were regenerated for 28.8 ks at 773 K under a 5 kPa O_2 in He stream with a total flow rate of 0.35 cm^3 s^{-1}. Organic product molar flow rates were quantified using a flame ionization detector on an Agilent 7890B gas chromatograph equipped with a methylsiloxane capillary column (HP-1, 30 m × 320 μm × 3 μm). Inorganic products were quantified using a thermal conductivity detector on the same GC setup connected to a bonded polystyrene−divinylbenzene (DVB) capillary column (HP-PLOT/Q, 30 m × 320 μm × 3 μm). *tert*-Butanol conversions were calculated by comparing total molar flow rates of carbon-containing products quantified using gas chromatography with inlet *tert*-butanol flow rates.

3. RESULTS AND DISCUSSION

3.1. Theory. Reduced cerium ions (Ce^{3+}:[Xe] $4f^1$), unlike oxidized ones (Ce^{4+}:[Xe]), carry an f electron beyond the closed shell configuration of Xenon; this f electron carries an orbital quantum number $l = 3$, magnetic quantum numbers $m_l = 3, 2, 1, 0, -1, -2, -3$, and spin quantum numbers $m_s = \pm^1/_2$, and can be accommodated within any one of seven 4f orbitals that each have two possible spin directions, resulting in 14 degenerate energy levels due to the absence of Coulombic interactions−energy levels that can collectively be expressed as a single ^2F term within the Russell−Saunders scheme,[44−46] where ^{M}L represents the term symbol with the following definitions:

$$\text{multiplicity, } M = 2S + 1 \quad (1)$$

https://doi.org/10.1021/acs.jpcc.2c06637
J. Phys. Chem. C 2023, 127, 234−247

$$\text{total spin angular momentum quantum number, } S = \sum_{i=1}^{N} m_{s_i} \tag{2}$$

$$\text{total orbital angular momentum quantum number, } L = \sum_{i=1}^{N} m_{l_i} \tag{3}$$

The f^1 electronic configuration of Ce^{3+} therefore results in a total spin value $S = {}^1/_2$, multiplicity $M = 2$, and total orbital quantum number $L = 3$, collectively denoted as ^2F. Interelectronic repulsion and spin−orbit coupling represent the two main perturbation contributions for electrons in an incompletely filled shell of a free ion, only the latter of which are manifested in the case of ions such as Ce^{3+}. Spin−orbit coupling effects break the degeneracy of the ^2F term and create two nondegenerate $^2F_{5/2}$ and $^2F_{7/2}$ states each with a corresponding $J = l + s$ value separated by 2200 cm^{-1} for a free Ce^{3+} ion (Scheme 1).[47−51] This $^2F_{5/2}$−$^2F_{7/2}$ transition therefore has associated with it a wavenumber that lies, fortuitously, within the infrared region of the electromagnetic spectrum, and may therefore be amenable to quantification using infrared techniques commonly employed in heterogeneous catalysis practice.[52] Crucially, splitting of energy levels consequent to its presence in a crystalline environment is expected to occur at much smaller energetic scales than that due to spin−orbit coupling effects,[49,53] implying that transitions between $Ce^{3+2}F_{5/2}$ and $^2F_{7/2}$ states may be observed within the infrared region not just for free ions present in the gas phase but also for ions hosted within bulk ceria domains commonly encountered either as active components or supports in heterogeneous catalysis applications. The presence of an electronic transition that lies within the infrared region of the electromagnetic spectrum appears to be rather unique to reduced cerium ions, as reflected by lanthanide ion Dieke diagrams capturing by line width the approximate extent of splitting in energy levels under crystalline environments (Figure S3, Supporting Information).[54] For example, Yb^{3+}, like Ce^{3+}, has $^2F_{5/2}$ and $^2F_{7/2}$ states, but instead with an energy difference (10,000 cm^{-1}) that lies outside the range of most infrared experiments (Figure S3, Supporting Information).

Over and above appearing in an energy range that can be probed using readily available experimental techniques, the transition, in order that it be detected experimentally, must also be nonforbidden within the scope of selection rules the results of which are determined by the crystal structure of the host solid. The forbidden nature of transitions in electronic absorption spectra can be ascertained using a transition moment integral term that describes the probability of occurrence of specific electronic transitions; more specifically, the La Porte selection rule stipulates that transitions between states of the same parity, i.e., symmetry with respect to a center of inversion, are forbidden, and this helps assess the intensity of absorption corresponding to an electronic transition based on the orbital component of wave functions present in the transition moment integral. The parity of a term symbol can be calculated as

$$P = (-1)^{\sum_i l_i} \tag{4}$$

where l_i is the orbital quantum number for each electron. The parity for both the $^2F_{5/2}$ and $^2F_{7/2}$ states is −1 (u), and hence the $^2F_{5/2} \rightarrow {}^2F_{7/2}$ electronic transition for a free Ce^{3+} ion in the gas phase is La Porte forbidden.[55] We posit that it is in fact the symmetry environment of bulk ceria catalysts and the effect of such a symmetry environment on electronic state parity that constitute the basis for this transition that is otherwise forbidden being experimentally observable.

The two energy levels under consideration, when present in a crystal environment that imposes an external electric field, will be further split into several Stark levels in a manner dependent on the point group of the symmetry environment as reflected in the spin−orbit quantum number J (Scheme 1)—a phenomenon referred to as the quadratic Stark effect.[49,56] Previous studies have used crystal field theory and group theory to evaluate how specific lattice site symmetries can result in $^2F_{5/2} \rightarrow {}^2F_{7/2}$ electronic transitions from ground to excited Stark levels being symmetrically nonforbidden, and they have also reported experimentally measured infrared bands for Ce^{3+} ions.[47,49,57] For example, Weber used infrared measurements of Ce^{3+} substituted into lattice sites of C_{1h} symmetry in $YAlO_3$ matrices to report energies of the four $^2F_{7/2}$ Stark levels as corresponding to wavenumbers of 2085, 2485, 2695, and 3250 cm^{-1} when considering a ground level energy value of zero.[47] Binet et al. report wavenumbers of these levels as 2021, 2067, 2104, and 2187 cm^{-1} for Ce^{3+} present in Ce(III) sulfate, whereas only one band at 2127 cm^{-1} was observed for H_2-treated cerous sulfate.[49] Similar symmetry allowed electronic transitions for Ce^{3+} ions have also been evidenced for other host crystals such as $LaCl_3$, CeF_3, CaF_2, $GdVO_4$, $LuVO_4$, $NaLaF_4$, $[Ca(PO_3)_2]_n$, $LiCaAlF_6$, and $BaLiF_3$, and for sites carrying symmetries including C_{1h}, D_{5h}, D_{3h}, C_{2v}, C_2, C_{3v}, and O_h.[48,51,58−60] Although the permissibility of Ce^{3+} electronic transitions has been assessed (using spectroscopic measurements) in the context of its presence in a variety of coordination environments, an understanding of the mathematical basis for its appearance in spectra, especially in cases where it appears in a C_{3v} site symmetry, remain poorly understood. Unlike Ce^{4+} ions in stoichiometric ceria samples that are characterized by a cubic O_h symmetry, the creation of oxygen vacancies facilitated by doping of trivalent rare earth cations has been suggested to place cerium sites into a C_{3v} symmetry, as evidenced using emission and excitation spectra[61−65] as well as electron paramagnetic resonance and an extended X-ray absorption fine structure (EXAFS) analysis.[66] It is worth noting that the C_{3v} point group is not the only symmetry environment in which Ce^{3+} ions are present on ceria surfaces, and that oxygen vacancies do not necessarily have to even be isolated in nature.[67] Considering the C_{3v} site symmetry environment, however, allows us to explain, from the standpoint of basic symmetry operations, the electronic transition corresponding to Ce^{3+} ions that happens to occur in the infrared region.

Considering specifically the C_{3v} site symmetry of Ce^{3+} ions in reduced ceria, we can use crystal field theory to assign a symmetry adopted form for each of the Stark levels. The reducible representation of 4f orbitals of a Ce^{3+} ion present in a C_{3v} crystal field can be expressed as follows (Section S2.3, Supporting Information):

$$\Gamma r = 2A_1 + A_2 + 2E \tag{5}$$

where Γr represents the reducible representation with three irreducible representations (IRs) A_1, A_2, and E of the C_{3v} point group. A_1 is a unidimensional IR that is symmetric with respect to the first and second symmetry elements of the point group,

https://doi.org/10.1021/acs.jpcc.2c06637
J. Phys. Chem. C 2023, 127, 234−247

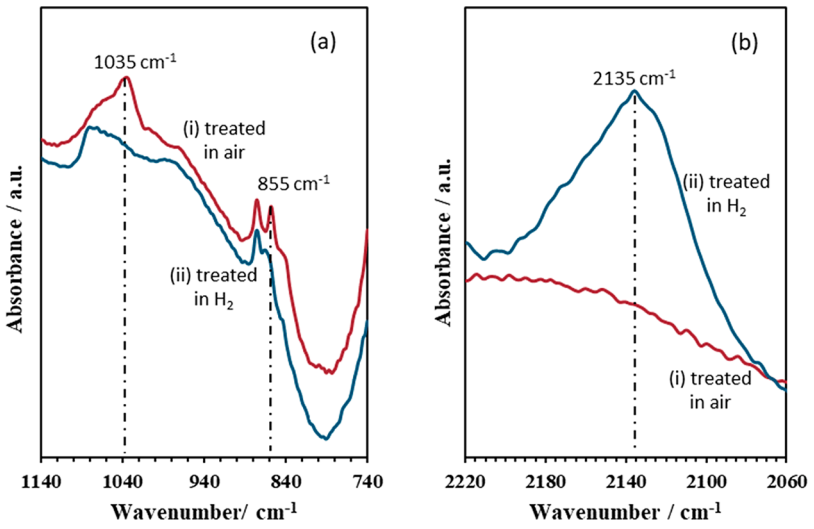

Figure 1. FTIR spectra of ceria samples (i) treated in air at 773 K (red) and (ii) treated in 13 kPa H_2 at 773 K (blue): (a) 740−1140 cm^{-1} region showing Ce═O stretching and Ce−O overtone mode bands; (b) 2060−2220 cm^{-1} region showing the $^2F_{5/2}$−$^2F_{7/2}$ electronic transition. Both sets of spectra were collected under N_2 flow at 323 K.

while A_2 is a unidimensional IR that is symmetric with respect to the first element, but not the second, and E represents a two-dimensional IR. The derivation of eq 5 (section S2.3, Supporting Information) captures the fact that the $^2F_{5/2}$ state is split into three nondegenerate states and the $^2F_{7/2}$ state is split into four states with 2-fold degeneracy, consistent with previously reported computational analysis and experimental absorption spectra for Ce^{3+} present in varying site symmetries.[47−49,57] Electronic transitions between ground and excited states will be IR active *if and only if* the transitions under consideration have (associated with them) nonzero transition moment integrals. The transition moment integral can be expressed as follows:

$$\text{transition moment integral} = \int \psi_i \cdot \vec{\mu} \cdot \psi_f \, d\tau \tag{6}$$

where ψ_i is the wave function of the initial state, ψ_f that of the final state, and $\vec{\mu}$ the dipole moment operator belonging to the representation describing the *x*, *y*, *z* basis set that for the C_{3v} group can be represented as $|\mu| = \begin{vmatrix} E \\ A_1 \end{vmatrix}$. The transition moment integral is nonzero when the direct product of two wave functions and the electric dipole moment operator contains a totally symmetric wave function A within the point group, which in the case of the C_{3v} point group corresponds to wave function A_1.

$$A_1 \rightarrow A_2,\ \psi_i \cdot |\mu| \cdot \psi_f = A_1 \cdot \begin{vmatrix} E \\ A_1 \end{vmatrix} \cdot A_2 \cdot \begin{vmatrix} E \\ A_1 \end{vmatrix} \cdot A_2 = \begin{vmatrix} E \\ A_2 \end{vmatrix};\ \text{forbidden}$$

$$A_1 \rightarrow E,\ \psi_i \cdot |\mu| \cdot \psi_f = A_1 \cdot \begin{vmatrix} E \\ A_1 \end{vmatrix} \cdot E = \begin{vmatrix} E \\ A_1 \end{vmatrix} \cdot E = \begin{vmatrix} A_1 + A_2 + E \\ E \end{vmatrix};\ \text{nonforbidden}$$

$$A_2 \rightarrow E,\ \psi_i \cdot |\mu| \cdot \psi_f = A_2 \cdot \begin{vmatrix} E \\ A_1 \end{vmatrix} \cdot E = \begin{vmatrix} E \\ A_2 \end{vmatrix} \cdot E = \begin{vmatrix} A_1 + A_2 + E \\ E \end{vmatrix};\ \text{nonforbidden}$$

There therefore exist two transitions—$A_1 \rightarrow E$ and $A_2 \rightarrow E$—that are nonforbidden by symmetry considerations and could potentially be observed experimentally. Experimental analyses reported previously in the literature support this finding in that well-defined bands have been observed in the vicinity of 2150 cm^{-1} in infrared measurements upon ceria reduction under H_2 as reported by the Sievers,[15] Weitz,[68] Binet,[49] Fornasiero,[69] Bonivardi,[70,71] Perez-Ramirez,[70] and Calatayud[71] groups; the Binet group noted an electronic transition at 2127 cm^{-1},[49] the Weitz group at 2147 cm^{-1},[68] the Sievers group at 2160 cm^{-1},[15] and Bonivardi and co-workers at 2120−2130 cm^{-1}.[70,71] More specifically, the Weitz group presented spectra in which the integrated intensity of the band at 2147 cm^{-1} tracked with the fraction of surface Ce^{3+} estimated using XPS when samples were reduced under H_2 between 250 and 650 °C.[68] Especially noteworthy is the fact that infrared bands reported in each of these prior studies lie in the vicinity of 2150 cm^{-1}, in close agreement with values suggested for separation of the two fundamental atomic levels in a free Ce^{3+} ion.[47−51,54] The rather close correspondence between the energetic separation of parent atomic levels from the final Stark levels can be explained by the shielding effect of valence 4f electrons of lanthanide rare-earth ions by filled 5s and 5p orbitals—an effect suggested to limit interaction of f electrons with the surrounding crystal environment,[54] implying a much lower extent of energy splitting due to electric fields corresponding to the crystalline environment than that due to spin−orbit coupling. Overall, group theory-based considerations suggest that the appearance, within the infrared region, of Ce^{3+} electronic transitions, can be rationalized on the basis of La Porte selection rules applied to the C_{3v} symmetry point group. In light of the wide-ranging catalytic implications of oxygen vacancy formation and concomitant Ce^{3+} formation, we present next a quantitative assessment of this electronic transition (in which we employ a variety of reductants and

https://doi.org/10.1021/acs.jpcc.2c06637
J. Phys. Chem. C 2023, 127, 234−247

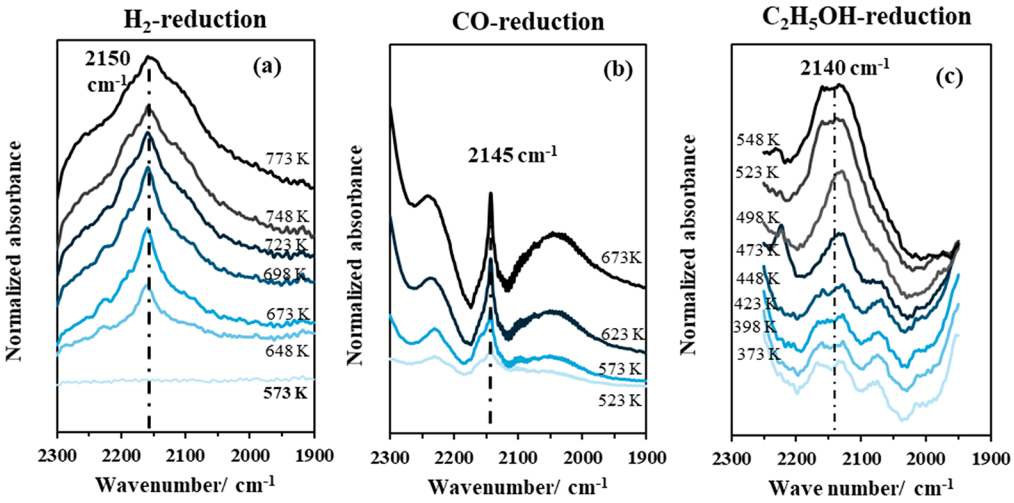

Figure 2. Infrared spectra of ceria samples normalized by the intensity of the Ce^{4+}=O stretching mode for the completely oxidized surface. Samples were reduced under (a) H_2, (b) CO, and (c) C_2H_5OH; background measurements for CO reduction experiments were conducted over oxidized ceria under 13 kPa CO at 473 K, and those for H_2 and ethanol were conducted under N_2 flow at 373 K. Reduction conditions: 13 kPa H_2/13 kPa CO/5.5 kPa C_2H_5OH, 9 kPa Ar, and balance N_2.

reduction conditions) toward estimating molar extinction coefficients.

3.2. Validation. High surface area cerium oxide (82 m^2/g) synthesized using literature-reported protocols[18] were characterized using X-ray diffraction, N_2 physisorption, and infrared spectroscopy. Measured diffraction patterns (Figure S1, Supporting Information) are consistent with the expected cubic structure and the associated *Fm*3*m* (225) space group, and N_2 physisorption isotherms (Figure S2, Supporting Information) reveal the presence of mesopores in the synthesized ceria sample. Figure 1 shows FTIR spectra measured at 323 K under N_2 flow after treatment at 773 K under either air or 13 kPa H_2. FTIR spectra measured after oxidative treatment under air at 773 K exhibit bands at 855 and 1035 cm^{-1} (Figure 1a) attributed, respectively, to terminal Ce^{4+}=O stretching and Ce−O overtone modes.[49,72,73] Reduction under 13 kPa H_2 at 773 K results in the disappearance of these bands and the concomitant appearance of a band at 2135 cm^{-1} (Figure 1b) that lies within the range of wavenumbers expected for the $^2F_{5/2}$−$^2F_{7/2}$ transition (2127−2160 cm^{-1} from previous studies[15,49,68]). This band was further analyzed quantitatively using three distinct reductants—H_2, CO, and ethanol. H_2 is the most commonly used reductant for ceria materials,[2,6,15,18,20,21,28,49,68,74,75] with prior studies suggesting 573 K as the reduction onset temperature for undoped cerium oxide[15] and the existence of two distinct temperature regimes for surface and bulk reduction in H_2−TPR experiments.[2] We intentionally limit experiments to reduction temperatures below 773 K in an effort to minimize complications arising out of bulk oxygen vacancy creation that become increasingly relevant at higher temperatures. CO shows marginally lower reduction onset temperatures than H_2 (513 K compared to 523 K),[28,74] and it appears to exhibit a more complex surface reduction mechanism that may include the incipient formation and decomposition of formate and carbonate species.[74,76] Vibrational fingerprints reported for these species with bands at 1375, 1580, 2845, and 2945 cm^{-1} for the formate species and 1300, 1385, 1485, and 1570 cm^{-1} for the carbonate species[76] do not overlap with the expected frequency for the Ce^{3+} electronic transition, and hence appear to permit quantitative analysis of bands associated with the latter. Ethanol was the third reductant used, with reduction temperatures restricted to a maximum of 573 K, below which reductive, not dehydrative, routes for ethanol conversion predominate.[6]

Figure 2 shows infrared absorbance spectra normalized to the stretching mode of terminal Ce=O bonds in the fully oxidized sample (855 cm^{-1}) as a function of reduction temperature for the three reductants under consideration. In situ spectra were obtained in the presence of reductants in the gas phase, with background measurements for H_2 and ethanol conducted under N_2 flow and those for CO conducted under 13 kPa CO flow at 473 K. CO_2 formation rates, and hence degrees of ceria surface reduction, remained imperceptibly low when exposing the sample to CO at 473 K, validating its use for background measurement purposes. Use of such a background spectrum was necessitated by the presence of a doublet at 2120 and 2175 cm^{-1} (Figure S4, Supporting Information) ascribed to P- and R-branches of vibrational−rotational absorption bands corresponding to gas phase CO[77−79]—a doublet that partially overlaps with the infrared band of interest at 2145 cm^{-1}. Despite using more complex background measurements, the doublet is not entirely eliminated (Figure 2b), and results in quantification of molar extinction coefficients using CO that are poorer in quality compared to those for H_2 and ethanol (*vide infra*).

Infrared bands for each of the three reductants were found to be centered in the 2140−2150 cm^{-1} range. Bands for experiments in which H_2 was used as reductant, however, appear at higher wavenumbers (2150 cm^{-1} versus 2145 and 2140 cm^{-1}), and are also significantly broader than those involving CO and ethanol as reductants (Figure 2). We surmise that the broader peaks measured under H_2 compared to the other two reductants are at least partly attributable to the higher reduction temperatures used for the former set of experiments. Temperature-dependent vibrational frequencies have previously been reported for 3d transition metal ions,[80] as well as 4f rare-earth ions such as Pr^{3+}[81] and Nd^{3+}.[82] Peak broadening may also be partly attributable to higher reduction temperatures used under H_2, in line with peak broadening effects for ceria reduction under H_2 reported by the Weitz group that appear to be amplified at higher temperatures.[68]

https://doi.org/10.1021/acs.jpcc.2c06637
J. Phys. Chem. C 2023, 127, 234−247

Peak broadening may also result from heterogeneity in cerium coordination environment, analogous to explanations for peak broadening based on the heterogeneity of Eu^{3+} coordination environment in glasses and sesquioxides.[83] Precise explanations for peak broadening remain outside the scope of this work, in which we instead limit discussion to the interpretation of integrated areas rather than the position or breadth of infrared bands.

Normalized integrated intensities for the electronic absorption peak, estimated by assuming the baseline to be a straight line between a fixed set of wavenumbers for each reductant used (H_2, 1925−2250 cm^{-1}; CO, 2115−2175 cm^{-1}; C_2H_5OH, 2050−2200 cm^{-1}), increase monotonically with vacancy densities estimated by quantifying rates of stoichiometric product formation (H_2O and CO_2) during isothermal reduction, with the sensitivity of integrated intensities to vacancy density being similar for all three reductants (Figure 3). Reduction under CO results in slightly lower sensitivities

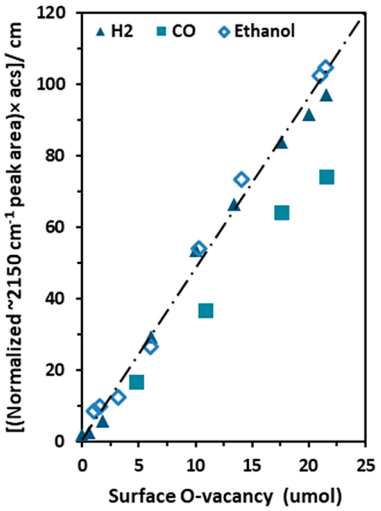

Figure 3. Integrated IR intensities normalized by the intensity of the band at 855 cm^{-1} (Ce−O stretching) as a function of oxygen vacancy density. The slope of this plot is proportional to the integrated molar extinction coefficient, *E*. Data obtained under CO was excluded when estimating the reported molar extinction coefficient.

compared to H_2 and ethanol, possibly due to errors resulting from the presence of doublets associated with gas-phase CO that necessitate more complex treatment of acquired infrared data. Overall, integrated areas vary linearly with vacancy density despite the breadth of measurement temperatures and reductants used, indicating that the identity of reductant as well as measurement temperature have little influence on molar extinction coefficients. Integrated molar extinction coefficients for Ce^{3+} sites were calculated using the equation:

$$E = {}^{A_{Ce^{3+}} \times a_{cs}} / n_{\text{O-vacancy}} \quad (7)$$

Here $A_{Ce^{3+}}$ represents the integrated area of the normalized infrared peak corresponding to the $^2F_{5/2} - {}^2F_{7/2}$ electronic transition, a_{cs} is the cross-sectional area of the wafer (1.1304 cm^2), and $n_{\text{O-vacancy}}$ represents the total micromoles of oxygen vacancies present in the IR cell under reduction conditions of interest. An integrated molar extinction coefficient value of 4.87 ± 0.16 cm $(\mu mol)^{-1}$ can be estimated for Ce^{3+} sites using H_2, and ethanol as reductants. Note that we exclude data corresponding to ceria reduction under CO that could potentially increase errors in integrated molar extinction coefficients estimated. We next use this extinction coefficient value to calculate (using eq 7) Ce^{3+} densities under reaction conditions where the latter are of interest yet remain unknown. Analysis of rate data in light of a quantitative understanding of vacancy densities appear to point to the involvement of reduced and oxidized ceria domains, respectively, in H_2-D_2 exchange and *tert*-butanol dehydration catalysis.

3.3. Application. *3.3.1. H_2-D_2 Exchange.* The dissociative adsorption of H_2 over reducible metal oxides is a key step of interest in a variety of catalytic reactions, select examples of which include alkyne semihydrogenation[84−86] and oxygenate hydrodeoxygenation.[15] In the case of reducible metal oxides specifically, oxygen vacancies have repeatedly been proposed as playing a role in effectuating the dissociative adsorption of H_2, in most cases using as evidence ex situ measurements of vacancy densities.[87−90] Rodriguez et al.,[87] for example, employed DFT to predict significantly lower energy barriers for H_2 dissociative adsorption over oxygen-deficient NiO surfaces compared to stoichiometric ones. They proposed oxygen vacancies as active centers for H_2 dissociation based on H_2 dissociation rates that increase with initial oxygen vacancy densities characterized using time-resolved XRD, EXAFS, and NEXAFS. Analogously, Song et al. used a linear correlation between 1-hexene hydrogenation rates at 313 K and oxygen vacancy concentrations measured using ex situ XPS analysis to suggest participation of oxygen vacancies in H_2 dissociation over reduced WO_3.[90] Two-step mechanisms for H_2 activation that are significantly more complex than the aforementioned ones have also been presented, an example of which are DFT-based proposals of the Zou group[88,89] in which H_2 dissociation over Co_3O_4 materials occurs through a multistep mechanism involving H_2 heterolytic scission forming Co−H and O−H species, followed by migration of the H atom from the Co-site to a separate O-site creating homolytic products. They propose that oxygen deficient surfaces resulted in weaker O−H bonds compared to stoichiometric ones, resulting in higher ethene hydrogenation rates over vacancy-enriched Co_3O_x surfaces. Similar two-step H_2 activation mechanisms comprised of initial heterolytic dissociation followed by H atom migration resulting in homolytic product formation have also been proposed by Garcia-Melchor et al. over stoichiometric ceria surfaces.[91] Albani et al., on the other hand, attributed the propensity of indium oxide surfaces toward alkyne semihydrogenation to the formation of a "single ensemble" comprised of an oxygen vacancy and a surrounding In_3O_5 unit that acts as the active center.[92]

In the case of ceria surfaces specifically, reports have claimed involvement of Ce^{3+}−lattice oxygen frustrated Lewis pairs in the heterolytic activation of H_2.[93−95] Zhang et al. reported increasing aromatic alkene and alkyne hydrogenation rates with surface Ce^{3+} density,[93] and Chang and co-workers used DFT analysis to suggest that frustrated Lewis pairs created upon ceria reduction stabilize Ce−H species, thereby significantly lowering activation barriers for acetylene hydrogenation over reduced ceria.[94] Lastly, Schimming et al. related H_2-D_2 exchange rates over pure and Zr-doped ceria to *ex situ* O_2 chemisorption-derived oxygen vacancy densities, providing strong evidence for the participation of vacancies in H_2 activation steps.

Our own data reinforce these inferences from previously published literature. Stoichiometric ceria samples exhibit imperceptibly low H_2-D_2 exchange rates at 423 K (9 kPa

https://doi.org/10.1021/acs.jpcc.2c06637
J. Phys. Chem. C 2023, 127, 234−247

H_2, 9 kPa D_2, 0.032 mol H_2 mol Ce_s^{-1} s^{-1}), unlike surfaces reduced under 13 kPa H_2 at 773 K that exhibit rates sufficient to achieve equilibrium H_2−D_2 conversion under identical reaction conditions (Figure S7, Supporting Information). In situ infrared spectra indicate, upon exposure to H_2−D_2 exchange conditions over stoichiometric surfaces, a barely perceptible band at 2693 cm^{-1} assigned previously to O−D species bridging two Ce^{4+} ions (IIA, Scheme 2 and Figure 4);[15]

Scheme 2. Different Types of Deuterated Hydroxyl Species on Oxidized and Reduced Ceria Surfaces and Their Expected Infrared Assignments[15,20]

	I-A site	*II-A site*	*II-B site*
Configuration	D–O–Ce^{4+}	D–O(–Ce^{4+})–O–Ce^{4+}	D–O(–Ce^{3+})–Ce^{3+}
Expected wavenumber (cm^{-1})	*2730*	*2693*	*2680*

H_2−D_2 exchange over prereduced ceria surfaces, on the other hand, result not in type IIA bridging hydroxyls but instead distinctly measurable bands at 2682 cm^{-1} assigned to hydroxyls bridging Ce^{3+} ions (Type IIB, Scheme 2) and at 2703 cm^{-1} assigned to either on-top (IA) or bridging (IIA) hydroxyls nonproximal to oxygen vacancies (Figure 4). The concurrent increase in bands corresponding to hydroxyls anticipated to be proximal as well as those nonproximal to oxygen vacancies are consistent with the formation of hydrogen species over oxygen species distinct in identity from those that facilitate H_2 dissociation in the first place, but it cannot exclude an alteration in propensity toward hydrogen activation of Ce^{4+} sites that are proximal to Ce^{3+} sites. More detailed mechanistic considerations such as these, as well as the nature of the formed hydrogen species (proton versus hydride versus hydrogen, for instance) remain outside the scope of this study, which instead focuses merely on presenting evidence for the involvement of reduced domains comprised of Ce^{3+} ions and oxygen vacancies in the activation of H_2 over ceria surfaces.

Many of the aforementioned literature reports, although providing strong evidence for the involvement of oxygen vacancies/Ce^{3+} ions in H_2 activation, rely either on theory or the ex situ characterization of vacancy densities to defend postulated mechanisms; quantitative, *in situ* application of the $^2F_{5/2}$ − $^2F_{7/2}$ infrared feature in estimating Ce^{3+} densities, if possible, would facilitate more direct experimental verification of their participation in hydrogen activation steps of relevance to hydrogenation and hydrodeoxygenation catalysis. A wide range of vacancy densities spanning degrees of surface reduction from 0.09 to 0.95 was accessed using reduction temperatures between 623 and 773 K. Forward rates of H_2−D_2 exchange at 373 K (9 kPa H_2, 9 kPa D_2, 0.032 mol H_2 mol Ce_s^{-1} s^{-1}) calculated using eqs 8 and 9 were found to vary linearly with vacancy density (Figure 5), providing strong supporting evidence for the involvement of Ce^{3+} ions in H_2−D_2 exchange catalysis and reinforcing interpretations presented previously in the literature using the ex situ characterization of

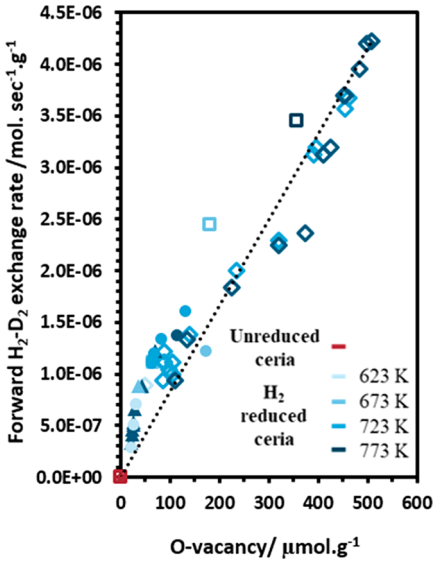

Figure 5. Forward rates of H_2−D_2 exchange at 373 K over reduced ceria samples. Different shapes (open squares, open diamonds, closed triangles, close circles) represent 4 distinct wafers on which experiments were conducted; reaction conditions: 373 K, 9 kPa H_2, 9 kPa D_2, 13.2 kPa Ar, and balance N_2.

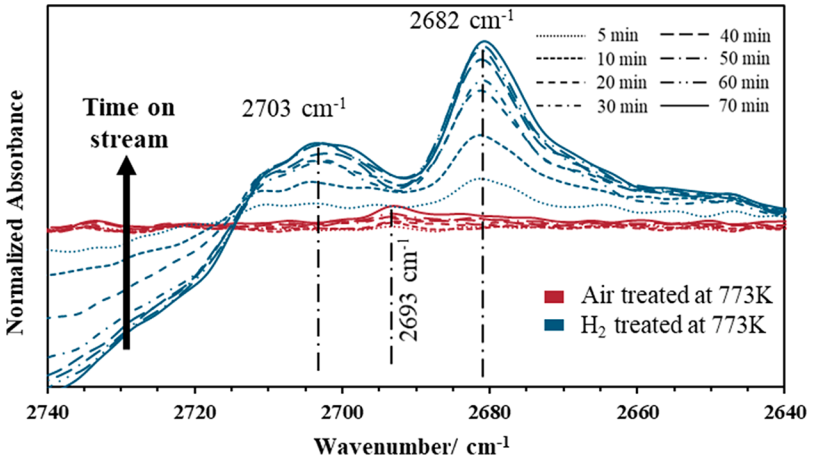

Figure 4. In situ FTIR spectra of ceria normalized by the intensity of the Ce^{4+}═O stretching mode corresponding to the completely oxidized surface under H_2−D_2 exchange conditions at 423 K over ceria surfaces oxidized at 773 K in air (red) and reduced at 773 K under 13 kPa H_2 (blue); reaction conditions: 9 kPa H_2, 9 kPa D_2, 13.2 kPa Ar, balance N_2, and 423 K.

https://doi.org/10.1021/acs.jpcc.2c06637
J. Phys. Chem. C 2023, 127, 234−247

vacancy densities. Higher H_2-D_2 exchange rates measured at lower vacancy densities would indicate a greater propensity for H−D exchange over isolated compared to clustered vacancies. Although forward exchange rates per vacancy below vacancy densities of 200 μmol g^{-1} appear to be higher than the average value estimated using the linear fit in Figure 5, it remains challenging to make definitive assertions in this respect from the data presented.

$$R_{net} = \vec{r}(1 - \eta) \tag{8}$$

$$\eta = \frac{C_{HD}^{\ 2}}{C_{H_2}.C_{D_2}}/K \tag{9}$$

where r_{net} represents the net rate of H_2-D_2 exchange, $\vec{r}$ the forward rate of exchange, η the approach to equilibrium, C_X the concentration of the respective species, and K the equilibrium constant for H_2-D_2 exchange. Quantification of vacancy densities using the method discussed here are in principle reliable even in the presence of reoxidation by minute quantities of water and O_2, unlike values estimated from oxygen balances the accuracy of which may be limited by the ability to reliably quantify water and/or oxygen molar flow rates. Initial vacancy densities estimated using ex situ techniques[87] and employed previously toward attribution of catalytic function could also be of rather limited utility under experimental conditions where vacancy densities evolve transiently. Utilization of the $^2F_{5/2}-^2F_{7/2}$ band, on the other hand, provides instantaneous, in situ measurements of vacancy densities that each require single spectral measurements unlike mass spectrometry-based analyses that require integration of oxygen imbalances over the time scale of interest, complications associated with which can obfuscate estimation of the degree of surface reduction, as shown next for an alkanol dehydration probe reaction.

3.3.2. tert-Butanol Dehydration. Ceria surfaces have been evaluated in a wide range of acid-catalyzed chemical transformations such as the hydrodeoxygenation of biomass-derived oxygenates;[5,6,15,18−21] specifically, alkanol dehydration has commonly been used as a probe reaction for deciphering the nature of acid sites on bulk metal oxides.[6,96−100] In an effort to better understand the roles of $Ce^{3+}-O^{2-}$ and $Ce^{4+}-O^{2-}$ pairs in alkanol dehydration catalysis, we employ toward dehydration catalysis *tert*-butanol—a probe molecule containing exclusively β, not α hydrogens—thereby circumventing complications resulting from the prevalence of stoichiometric and catalytic alkanol dehydrogenation routes the occurrence over ceria surfaces of which have been evidenced and contributions of which have been analyzed quantitatively in a previously published study.[6]

Isobutene and CO_2 are the only two carbon-containing products detected upon feeding *tert*-butanol over bulk ceria at 433 K, with the higher oxygen:carbon ratio in CO_2 compared to *tert*-butanol necessarily implying the creation of oxygen vacancies upon formation of the former. Isobutene and CO_2 formation rates decrease monotonically with time-on-stream with only minimal concomitant changes in product selectivity (Figure 6), suggesting a proportionate decrease in the number of active sites available for both reactions upon extraction of surface oxygen. Vacancy densities can be calculated using the stoichiometry of the oxidation reaction: the oxidation of *tert*-butanol to CO_2 and water, either in primary oxidation steps or through deep oxidation steps involving the formation and

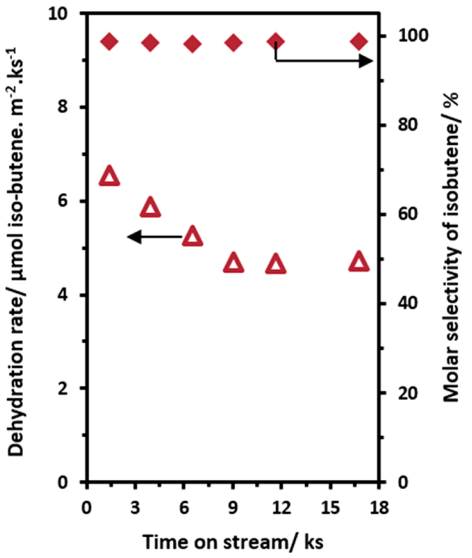

Figure 6. *tert*-Butanol dehydration rate and product selectivity versus time on stream. Reaction conditions: 0.28 kPa *tert*-butanol, balance He, 433 K, and 0.042 mol *tert*-butanol (mol $Ce_s)^{-1}$ s^{-1}.

subsequent reaction of isobutene, involve the extraction of three surface oxygens per molecule of *tert*-butanol reacted (Scheme 3, eq 10). Vacancy densities calculated using eq 10

Scheme 3. Reaction Stoichiometry for Total Oxidation of *tert*-Butanol (Top) and Isobutene (Bottom) with the Involvement of Surface Oxygens (Os) and the Formation of Oxygen Vacancies (V_O)

$$C_4H_9OH + 12O_s \rightarrow 4CO_2 + 5H_2O + 12V_O$$

$$C_4H_8 + 12O_s \rightarrow 4CO_2 + 4H_2O + 12V_O$$

increase monotonically with time-on-stream for the first 18 ks (Figure 7a), in contrast with isobutene formation rates (and hence site densities) that initially decrease before leveling out at their steady state values (Figure 6), pointing to the inaccurate nature of vacancy densities calculated using eq 10, presumably due to reoxidation of surfaces resulting from water formation in dehydration and oxidation reactions. In situ characterization techniques that probe prevalent Ce^{3+} densities directly without recourse to accurate CO_2 and H_2O product formation rates—rates that are highly challenging to measure given their exceedingly low selectivities (<2 mol % CO_2)—are therefore needed to rationalize site requirements for *tert*-butanol dehydration.

$$\text{moles of O-vacancies created} = 3 \times \text{cumulative moles of } CO_2 \text{ formed} \tag{10}$$

In situ infrared spectra measured during the *tert*-butanol dehydration transient indicate increasing areas of the band at 2135 cm^{-1} (assigned to the presence of Ce^{3+} ions) with time-on-stream (Figure 8), indicating surface reduction, presumably as a consequence of *tert*-butanol oxidation to CO_2. Vacancy densities calculated using eq 7 and a molar extinction coefficient value of 4.87 cm $(\mu mol)^{-1}$ estimated in section 3.2 were found to level off at a steady state value of 0.035 mol vacancies per mol of initial surface oxygen (Figure 7b), unlike

https://doi.org/10.1021/acs.jpcc.2c06637
J. Phys. Chem. C 2023, 127, 234−247

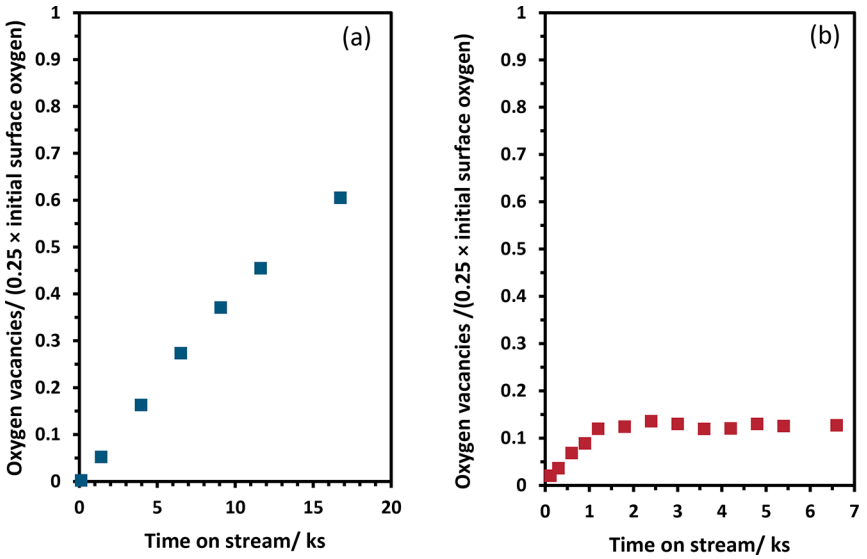

Figure 7. Normalized vacancy densities during *tert*-butanol dehydration over high surface area ceria (a) calculated using eq 10. reaction conditions: 0.28 kPa *tert*-butanol, balance He, 433 K, ambient pressure, and 0.042 mol *tert*-butanol (mol Ce_s)$^{-1}$ s^{-1}. (b) Estimated from in situ infrared data. Reaction conditions: 40 mg of catalyst wafer with 25 mg CaF_2, 0.28 kPa *tert*-butanol in N_2, 433 K, and 0.035 mol of *tert*-butanol (mol Ce_s)$^{-1}$ s^{-1}.

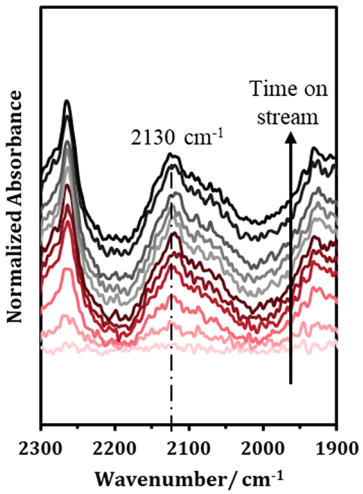

Figure 8. In situ FTIR spectra normalized by the intensity of the Ce^{4+}═O stretching mode for a fully oxidized surface. Spectra were collected during *tert*-butanol dehydration catalysis; reaction conditions: 40 mg of catalyst wafer with 25 mg of CaF_2, 0.28 kPa *tert*-butanol in N_2, 433 K, and 0.035 mol of *tert*-butanol (mol Ce_s)$^{-1}$ s^{-1}.

those calculated from eq 10 that keep increasing monotonically with time-on-stream, consistent with the prevalence of H_2O-mediated surface reoxidation resulting in an overestimation of site densities calculated from CO_2 product formation rates; estimation of vacancy densities using eq 7, unlike eq 10, are unaffected by the extent of product-mediated reoxidation events, and in all likelihood provide more rigorous estimates of Ce^{3+}/oxygen vacancy site densities. The leveling off of infrared-derived vacancy densities offers an explanation for the achievement of steady state dehydration rates as shown in Figure 6, and it also suggests that controlling vacancy densities may provide a means for tuning steady state dehydration rates.

Unlike H_2−D_2 exchange reactions, high temperature H_2-treatments cannot be used directly to control vacancy densities during dehydration catalysis owing to surface reoxidation by water formed as byproduct. We postulate that cofeeding α hydrogen-containing alkanols such as ethanol will result in larger vacancy densities than those achievable without cofeeds; ethanol, unlike *tert*-butanol, has a propensity to participate in oxidative routes at 433 K and carries an ability to reduce ceria surfaces at sufficiently low temperatures (373−548 K).[6,16,101] Steady state isobutene formation rates decrease, while oxygen vacancy densities increase monotonically with increasing ethanol cofeed pressure (Figure S11, Supporting Information), consistent with decreasing dehydration site densities with increasing ethanol cofeed pressure and the occurrence of *tert*-butanol dehydration catalysis over oxidized domains; steady state dehydration rates are likely determined by a balance between the rates of oxidation of ethanol and *tert*-butanol on the one hand, and those of reoxidation of ceria surfaces by water generated in both dehydration and oxidation reactions. Dehydration reactions produce water molecules that partially reoxidize the surface, unlike oxidation reactions that both reduce and oxidize the surface. Ethanol contributes predominantly to oxidative pathways, resulting in significantly higher vacancy densities and lower steady state dehydration rates at higher ethanol cofeed pressures (Figure 9). The more rapid approach to steady state degrees of surface reduction at higher ethanol cofeed pressures (Figure S11b) is also consistent with induction periods representing time scales required for achieving a balance between oxidation rates (predominantly contributed by ethanol) and dehydration rates (predominantly contributed by *tert*-butanol). Overall, the strong inverse correlation between dehydration rates and infrared derived vacancy densities (Figure 9) suggest participation of oxidized domains in *tert*-butanol dehydration catalysis, and reemphasize the utility of a quantitative analysis of the $Ce^{3+2}F_{5/2}$−$^2F_{7/2}$ transition in elucidating active site requirements in ceria catalysis.

CONCLUSIONS

$^2F_{5/2}$ → $^2F_{7/2}$ electronic transitions for Ce^{3+} ions in a C_{3v} symmetry environment, unlike those for free ions in the gas phase, are La Porte nonforbidden, as evidenced by their nonzero transition moment integrals. This transition, which

https://doi.org/10.1021/acs.jpcc.2c06637
J. Phys. Chem. C 2023, 127, 234−247

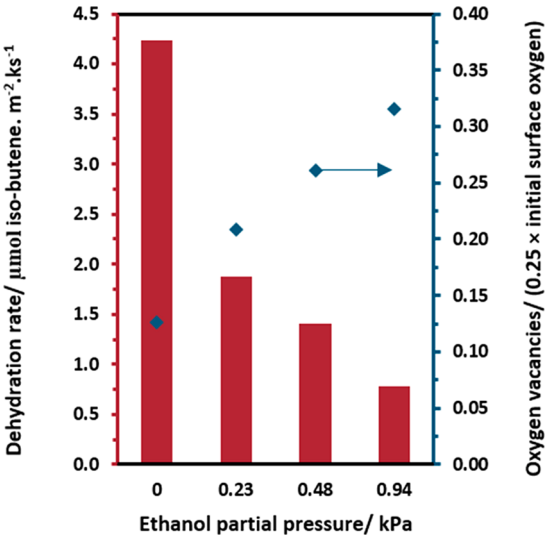

Figure 9. Steady state isobutene formation rates and normalized oxygen vacancy densities as a function of ethanol cofeed pressure. Reaction conditions: 0.28 kPa *tert*-butanol, 0.23/0.48/0.94 kPa C_2H_5OH, balance He, and 433 K.

lies (fortuitously) in the infrared region of the electromagnetic spectrum, is amenable to quantitative use, as demonstrated by the measurement of molar extinction coefficient values that are reproducible in nature regardless of the identity of reductants used and oxidation products produced. The role of Ce^{3+} ions/oxygen vacancies in hydrogen activation previously proposed using ex situ characterization methods are captured here through the in situ quantification of infrared contributions of the $^2F_{5/2} \rightarrow {}^2F_{7/2}$ transition, with a linear correlation between forward H_2-D_2 exchange rates and infrared-derived vacancy densities providing strong evidence for the favorable effect of surface reduction on hydrogen activation specifically and hydrogenation/hydrodeoxygenation reactions more generally. Quantitative analysis of the infrared feature corresponding to this electronic transition also aids in the rationalization of steady state *tert*-butanol dehydration rate data both in the presence and absence of ethanol cofeeds carrying a propensity for surface oxidation. Rationalization of induction periods and steady state rate data based on product formation rates rather than infrared spectroscopy appear to be more cumbersome (and potentially infeasible) owing to water-mediated reoxidation of ceria surfaces that significantly complicate rate data interpretation, and emphasize the utility of direct, in situ assessments of vacancy densities in elucidating site requirements in ceria catalysis. The nonforbidden nature of this transition appears to extend beyond the specific C_{3v} site symmetry environment under consideration here, and could potentially find utility in the rigorous quantification of vacancy densities and facilitation of structure−catalytic property relationship development in ceria catalysis more broadly.

■ ASSOCIATED CONTENT

Supporting Information

The Supporting Information is available free of charge at https://pubs.acs.org/doi/10.1021/acs.jpcc.2c06637.

Details of materials characterization, including powder X-ray diffraction and N_2-physisorption, derivation of the reducible representation, normalization of Ce^{3+} bands with that corresponding to Ce═O stretching, and details of H_2-D_2 exchange and *tert*-butanol dehydration experiments (PDF)

■ AUTHOR INFORMATION

Corresponding Author

Praveen Bollini − *Department of Chemical & Biomolecular Engineering, University of Houston, Houston, Texas 77004, United States;* orcid.org/0000-0001-8092-8092; Email: ppbollini@uh.edu

Author

Sadia Afrin − *Department of Chemical & Biomolecular Engineering, University of Houston, Houston, Texas 77004, United States*

Complete contact information is available at: https://pubs.acs.org/10.1021/acs.jpcc.2c06637

Notes

The authors declare no competing financial interest.

■ ACKNOWLEDGMENTS

The authors acknowledge support from the National Science Foundation (Award No. 1916133).

■ REFERENCES

(1) Reinhardt, K.; Winkler, H.*Cerium Mischmetal, Cerium Alloys, and Cerium Compounds*; Wiley-VCH: Weinheim, Germany, 2012; Vol. *8*, DOI: 10.1002/14356007.a06.

(2) Yao, H. C.; Yao, Y. F. Y. Ceria in Automotive Exhaust Catalysts. I. Oxygen Storage. *J. Catal.* **1984**, *86* (2), 254−265.

(3) Trovarelli, A. Catalytic Properties of Ceria. *Catal. Rev.* **1996**, *38*, 439−520.

(4) Vivier, L.; Duprez, D. Ceria-Based Solid Catalysts for Organic Chemistry. *ChemSusChem* **2010**, *3* (6), 654−678.

(5) Afrin, S.; Bollini, P. Cerium Oxide Catalyzes the Selective Vapor-Phase Hydrodeoxygenation of Anisole to Benzene at Ambient Pressures of Hydrogen. *Ind. Eng. Chem. Res.* **2019**, *58* (31), 14603−14607.

(6) Afrin, S.; Bollini, P. A Transient Kinetic Analysis of the Evolution of a Reducible Metal Oxide towards Catalyzing Nonoxidative Alkanol Dehydrogenation. *J. Catal.* **2021**, *393*, 290−302.

(7) Al-Shankiti, I.; Al-Otaibi, F.; Al-Salik, Y.; Idriss, H. Solar Thermal Hydrogen Production from Water over Modified CeO_2 Materials. *Top. Catal.* **2013**, *56* (12), 1129−1138.

(8) Ziemba, M.; Stark, D.; Hess, C. Combined DFT and Operando Spectroscopic Study of the Water-Gas Shift Reaction over Ceria-Based Catalysts: The Role of the Noble Metal and Ceria Faceting. *Chem. Proc.* **2020**, *2* (1), 23.

(9) Hilaire, S.; Wang, X.; Luo, T.; Gorte, R. J.; Wagner, J. A Comparative Study of Water-Gas-Shift Reaction over Ceria-Supported Metallic Catalysts. *Appl. Catal. A Gen.* **2004**, *258* (2), 271−276.

(10) Karpenko, A.; Leppelt, R.; Plzak, V.; Cai, J.; Chuvilin, A.; Schumacher, B.; Kaiser, U.; Behm, R. J. Influence of the Catalyst Surface Area on the Activity and Stability of Au/CeO_2 Catalysts for the Low-Temperature Water Gas Shift Reaction. *Top. Catal.* **2007**, *44* (1−2), 183−198.

(11) Zhang, D.; Du, X.; Shi, L.; Gao, R. Shape-Controlled Synthesis and Catalytic Application of Ceria Nanomaterials. *Dalt. Trans.* **2012**, *41* (48), 14455−14475.

(12) Agarwal, S.; Lefferts, L.; Mojet, B. L.; Ligthart, D. A. J. M.; Hensen, E. J. M.; Mitchell, D. R. G.; Erasmus, W. J.; Anderson, B. G.; Olivier, E. J.; Neethling, J. H.; et al. Exposed Surfaces on Shape-Controlled Ceria Nanoparticles Revealed through AC-TEM and Water-Gas Shift Reactivity. *ChemSusChem* **2013**, *6* (10), 1898−1906.

(13) Schilling, C.; Hofmann, A.; Hess, C.; Ganduglia-Pirovano, M. V. Raman Spectra of Polycrystalline CeO_2: A Density Functional Theory Study. *J. Phys. Chem. C* **2017**, *121* (38), 20834−20849.
(14) Filtschew, A.; Hofmann, K.; Hess, C. Ceria and Its Defect Structure: New Insights from a Combined Spectroscopic Approach. *J. Phys. Chem. C* **2016**, *120* (12), 6694−6703.
(15) Schimming, S. M.; Foo, G. S.; Lamont, O. D.; Rogers, A. K.; Yung, M. M.; D'Amico, A. D.; Sievers, C. Kinetics of Hydrogen Activation on Ceria-Zirconia. *J. Catal.* **2015**, *329*, 335−347.
(16) Li, M.; Wu, Z.; Overbury, S. H. Surface Structure Dependence of Selective Oxidation of Ethanol on Faceted CeO_2 Nanocrystals. *J. Catal.* **2013**, *306*, 164−176.
(17) Nolan, M.; Parker, S. C.; Watson, G. W. The Electronic Structure of Oxygen Vacancy Defects at the Low Index Surfaces of Ceria. *Surf. Sci.* **2005**, *595* (1−3), 223−232.
(18) Schimming, S. M.; Lamont, O. D.; König, M.; Rogers, A. K.; D'Amico, A. D.; Yung, M. M.; Sievers, C. Hydrodeoxygenation of Guaiacol over Ceria-Zirconia Catalysts. *ChemSusChem* **2015**, *8* (12), 2073−2083.
(19) Vohs, J. M. Site Requirements for the Adsorption and Reaction of Oxygenates on Metal Oxide Surfaces. *Chem. Rev.* **2013**, *113* (6), 4136−4163.
(20) Binet, C.; Daturi, M.; Lavalley, J. C. IR Study of Polycrystalline Ceria Properties in Oxidised and Reduced States. *Catal. Today* **1999**, *50* (2), 207−225.
(21) El Fallah, J.; Boujana, S.; Dexpert, H.; Kiennemann, A.; Majerus, J.; Touret, O.; Villain, F.; Le Normand, F. Redox Processes on Pure Ceria and on Rh/CeO_2 Catalyst Monitored by X-Ray Absorption (Fast Acquisition Mode). *J. Phys. Chem.* **1994**, *98* (21), 5522−5533.
(22) Ferrizz, R. M.; Wong, G. S.; Egami, T.; Vohs, J. M. Structure Sensitivity of the Reaction of Methanol on Ceria. *Langmuir* **2001**, *17* (8), 2464−2470.
(23) Zhao, C.; Watt, C.; Kent, P. R.; Overbury, S. H.; Mullins, D. R.; Calaza, F. C.; Savara, A.; Xu, Y. Coupling of Acetaldehyde to Crotonaldehyde on CeO_{2-x} (111): Bifunctional Mechanism and Role of Oxygen Vacancies. *J. Phys. Chem. C* **2019**, *123* (13), 8273−8286.
(24) Calaza, F. C.; Xu, Y.; Mullins, D. R.; Overbury, S. H. Oxygen Vacancy-Assisted Coupling and Enolization of Acetaldehyde on CeO_2(111). *J. Am. Chem. Soc.* **2012**, *134* (43), 18034−18045.
(25) Reimers, W. G.; Baltanás, M. A.; Branda, M. M. Theoretical Study on the Reactivity of the Surface of Pure Oxides: The Influence of the Support and Oxygen Vacancies. *Appl. Surf. Sci.* **2013**, *274*, 1−6.
(26) Wu, Z.; Mann, A. K. P.; Li, M.; Overbury, S. H. Spectroscopic Investigation of Surface Dependent Acid Base Property of Ceria Nanoshapes. *J. Phys. Chem. C* **2015**, *119* (13), 7340−7350.
(27) Madier, Y.; Descorme, C.; Le Govic, A. M.; Duprez, D. Oxygen Mobility in CeO_2 and $Ce_xZr_{(1-x)}O_2$ Compounds: Study by CO Transient Oxidation And18O/16O Isotopic Exchange. *J. Phys. Chem. B* **1999**, *103* (50), 10999−11006.
(28) Trovarelli, A. Catalytic Properties of Ceria and CeO_2-Containing Materials. *Catal. Rev. - Sci. Eng.* **1996**, *38* (4), 439−520.
(29) Qiu, L.; Liu, F.; Zhao, L.; Ma, Y.; Yao, J. Comparative XPS Study of Surface Reduction for Nanocrystalline and Microcrystalline Ceria Powder. *Appl. Surf. Sci.* **2006**, *252* (14), 4931−4935.
(30) Reddy, B. M.; Khan, A.; Yamada, Y.; Kobayashi, T.; Loridant, S.; Volta, J. C. Structural Characterization of CeO_2-MO_2 (M = Si^{4+}, Ti^{4+}, and Zr^{4+}) Mixed Oxides by Raman Spectroscopy, x-Ray Photoelectron Spectroscopy, and Other Techniques. *J. Phys. Chem. B* **2003**, *107* (41), 11475−11484.
(31) Yang, Y.; Mao, Z.; Huang, W.; Liu, L.; Li, J.; Li, J.; Wu, Q. Redox Enzyme-Mimicking Activities of CeO_2 Nanostructures: Intrinsic Influence of Exposed Facets. *Sci. Rep.* **2016**, *6*, 1−7.
(32) Choi, Y. M.; Abernathy, H.; Chen, H. T.; Lin, M. C.; Liu, M. Characterization of O_2-CeO_2 Interactions Using in Situ Raman Spectroscopy and First-Principle Calculations. *ChemPhysChem* **2006**, *7* (9), 1957−1963.
(33) Wu, Z.; Li, M.; Howe, J.; Meyer, H. M.; Overbury, S. H. Probing Defect Sites on CeO_2 nanocrystals with Well-Defined Surface Planes by Raman Spectroscopy and O_2 adsorption. *Langmuir* **2010**, *26* (21), 16595−16606.
(34) Li, L.; Chen, F.; Lu, J. Q.; Luo, M. F. Study of Defect Sites in $Ce_{1-x}M_xO_{2-\delta}$(x = 0.2) Solid Solutions Using Raman Spectroscopy. *J. Phys. Chem. A* **2011**, *115* (27), 7972−7977.
(35) Taniguchi, T.; Watanabe, T.; Sugiyama, N.; Subramani, A. K.; Wagata, H.; Matsushita, N.; Yoshimura, M. Identifying Defects in Ceria-Based Nanocrystals by UV Resonance Raman Spectroscopy. *J. Phys. Chem. C* **2009**, *113* (46), 19789−19793.
(36) Li, C.; Domen, K.; Maruya, K. I.; Onishi, T. Dioxygen Adsorption on Well-Outgassed and Partially Reduced Cerium Oxide Studied by FT-IR. *J. Am. Chem. Soc.* **1989**, *111* (20), 7683−7687.
(37) Li, C.; Domen, K.; Maruya, K. I.; Onishi, T. Oxygen Exchange Reactions over Cerium Oxide: An FT-IR Study. *J. Catal.* **1990**, *123* (2), 436−442.
(38) Padeste, C.; Cant, N. W.; Trimm, D. L. Influence of Water on the Reduction and Reoxidation Ofceria. *Catal Lett.* **1993**, *18*, 305−316.
(39) Wu, Z.; Li, M.; Mullins, D. R.; Overbury, S. H. Probing the Surface Sites of CeO_2 Nanocrystals with Well-Defined Surface Planes via Methanol Adsorption and Desorption. *ACS Catal.* **2012**, *2* (11), 2224−2234.
(40) Soria, J.; Coronado, J. M.; Conesa, J. C. Spectroscopic Study of Oxygen Adsorption on CeO_2/γ-Al_2O_3 Catalyst Supports. *J. Chem. Soc. - Faraday Trans.* **1996**, *92* (9), 1619−1626.
(41) Wang, L.; Wang, Y.; Zhang, Y.; Yu, Y.; He, H.; Qin, X.; Wang, B. Shape Dependence of Nanoceria on Complete Catalytic Oxidation of O-Xylene Electronic Supplementary Information. *Catal. Sci. Technol.* **2016**, *6*, 4840−4848.
(42) DeWilde, J. F.; Chiang, H.; Hickman, D. A.; Ho, C. R.; Bhan, A. Kinetics and Mechanism of Ethanol Dehydration on γ-Al_2O_3: The Critical Role of Dimer Inhibition. *ACS Catal.* **2013**, *3* (4), 798−807.
(43) Rossignol, S.; Madier, Y.; Duprez, D. Preparation of Zirconia-Ceria Materials by Soft Chemistry. *Catal. Today* **1999**, *50* (2), 261−270.
(44) Meena, P. L.; Kumar, N.; Meena, A. S.; Meena, K. S. Comparative Studies on Russell-Saunders Atomic Term Symbols (Terms) for Equivalent Electrons of Nf4 and Nf10 Configurations. *Bulg. Chem. Commun.* **2014**, *46* (1), 141−149.
(45) Freidzon, A. Y.; Kurbatov, I. A.; Vovna, V. I. Ab Initio Calculation of Energy Levels of Trivalent Lanthanide Ions. *Phys. Chem. Chem. Phys.* **2018**, *20*, 14564−14577.
(46) Hyde, K. E. Methods for Obtaining Russell-Saunders Term Symbols from Electronic Configurations. *J. Chem. Educ.* **1975**, *52* (2), 87−89.
(47) Weber, M. J. Optical Spectra of Ce^{3+} and Ce^{3+} -Sensitized Fluorescence in $YAlO_3$. *J. Appl. Phys.* **1973**, *44* (7), 3205−3208.
(48) Buchanan, R. A.; Rast, H. E.; Caspers, H. H. Infrared Absorption of Ce^{3+} in LaF_3 and of CeF_3. *J. Chem. Phys.* **1966**, *44* (11), 4063−4065.
(49) Binet, C.; Badri, A.; Lavalley, J. C. A Spectroscopic Characterization of the Reduction of Ceria from Electronic Transitions of Intrinsic Point Defects. *J. Phys. Chem.* **1994**, *98* (25), 6392−6398.
(50) Yamaga, M; Imai, T; Shimamura, K; Fukuda, T; Honda, M Optical Spectroscopy of Ce^{3+} in $BaLiF_3$. *J. Phys. Condens. Matter* **2000**, *12*, 3431−3439.
(51) Yamaga, M.; Lee, D.; Henderson, B.; Han, T. P. J.; Gallagher, H. G.; Yosida, T. The Magnetic and Optical Properties of Ce^{3+} in $LiCaAlF_6$. *J. Phys.: Condens. Matter* **1998**, *10* (14), 3223−3237.
(52) Savara, A.; Weitz, E. Elucidation of Intermediates and Mechanisms in Heterogeneous Catalysis Using Infrared Spectroscopy. *Annu. Rev. Phys. Chem.* **2014**, *65*, 249−273.
(53) Elliott, J.; Judd, B. R.; Runciman, W. Energy Levels in Rare-Earth Ions. *Proc. R. Soc. London. Ser. A. Math. Phys. Sci.* **1957**, *240*, 509−523.
(54) Sorokina, I. T.*Crystalline Mid-Infrared Lasers*; Springer: Berlin and Heidelberg, Germany, 2003. DOI: 10.1007/3-540-36491-9.

(55) Ofelt, G. S. Intensities of Crystal Spectra of Rare-Eart(1) Ofelt, G. S. Intensities of Crystal Spectra of Rare-Earth Ions. *J. Chem. Phys.* **1962**, *37* (3), 511−520; Ions. *J. Chem. Phys.* **1962**, *37* (3), 511−520.
(56) Bünzli, J.-C. G.; Eliseeva, S. V.*Basics of Lanthanide Photophysics*; Springer: Berlin and Heidelberg, Germany, 2010; DOI: 10.1007/4243_2010_3.
(57) Carnall, W. T.; Goodman, G. L.; Rajnak, K.; Rana, R. S. A Systematic Analysis of the Spectra of the Lanthanides Doped into Single Crystal LaF_3. *J. Chem. Phys.* **1989**, *90* (7), 3443−3457.
(58) Weber, M. J.; Bierig, R. W. Paramagnetic Resonance and Relaxation of Trivalent Rare-Earth Ions in Calcium Fluoride. I. Resonance Spectra and Crystal Fields. *Phys. Rev.* **1964**, *134* (6A), A1492−A1503.
(59) Krumpel, A. H.*Locating Energy Levels of Lanthanide Ions in Inorganic Ionic Compounds*; Shaker Publishing: Maastricht, The Netherlands, 2009.
(60) Das Mohapatra, G. K. A Spectroscopic Study of Ce^{3+} Ion in Calcium Metaphosphate Glass. *Phys. Chem. Glas.* **1998**, *39* (1), 50−55.
(61) Linares, R. C. Fluorescent Properties of Trivalent Rare Earths in Fluorite Structure Oxides. *J. Opt. Soc. Am.* **1966**, *56* (12), 1700.
(62) Yin, M.; Krupa, J.-C.; Antic-Fidancev, E.; Lorriaux-Rubbens, A. Spectroscopic Studies of Eu^{3+} and Dy^{3+} Centers in ThO_2. *Phys. Rev. B* **2000**, *61* (12), 8073−8080.
(63) Tiseanu, C.; Parvulescu, V. I.; Sanchez-Dominguez, M.; Boutonnet, M. Temperature Induced Conversion from Surface to Bulk Sites in Eu_3-Impregnated CeO_2 Nanocrystals. *J. Appl. Phys.* **2012**, *112* (1), 013521.
(64) Murgida, G. E.; Ferrari, V.; Llois, A. M.; Ganduglia-Pirovano, M. V. Reduced CeO2(111) Ordered Phases as Bulk Terminations: Introducing the Structure of Ce_3O_5. *Phys. Rev. Mater.* **2018**, *2* (8), 1−10.
(65) Kumar, S.; Schelling, P. K. Density Functional Theory Study of Water Adsorption at Reduced and Stoichiometric Ceria (111) Surfaces. *J. Chem. Phys.* **2006**, *125* (20), 204704.
(66) Korobko, R.; Lerner, A.; Li, Y.; Wachtel, E.; Frenkel, A. I.; Lubomirsky, I. In-Situ Extended X-Ray Absorption Fine Structure Study of Electrostriction in Gd Doped Ceria. *Appl. Phys. Lett.* **2015**, *106* (4), 042904.
(67) Wolf, M. J.; Castleton, C. W. M.; Hermansson, K.; Kullgren, J. STM Images of Anionic Defects at CeO_2(111)-A Theoretical Perspective. *Front. Chem.* **2019**, *7*, 1−11.
(68) Wu, W.; Savereide, L. M.; Notestein, J.; Weitz, E. In-Situ IR Spectroscopy as a Probe of Oxidation/Reduction of Ce in Nanostructured CeO_2. *Appl. Surf. Sci.* **2018**, *445*, 548−554.
(69) Gennari, F. C.; Montini, T.; Hickey, N.; Fornasiero, P.; Graziani, M. IR Investigation of the Interaction of Deuterium with $Ce_{0.6}Zr_{0.4}O_2$ and Cl-Doped $Ce_{0.6}Zr_{0.4}O_2$. *Appl. Surf. Sci.* **2006**, *252* (24), 8456−8465.
(70) Vilé, G.; Dähler, P.; Vecchietti, J.; Baltanás, M.; Collins, S.; Calatayud, M.; Bonivardi, A.; Pérez-Ramírez, J. Promoted Ceria Catalysts for Alkyne Semi-Hydrogenation. *J. Catal.* **2015**, *324*, 69−78.
(71) Vecchietti, J.; Baltanás, M. A.; Gervais, C.; Collins, S. E.; Blanco, G.; Matz, O.; Calatayud, M.; Bonivardi, A. Insights on Hydride Formation over Cerium-Gallium Mixed Oxides: A Mechanistic Study for Efficient H_2 Dissociation. *J. Catal.* **2017**, *345*, 258−269.
(72) Burow, A. M.; Wende, T.; Sierka, M.; Włodarczyk, R.; Sauer, J.; Claes, P.; Jiang, L.; Meijer, G.; Lievens, P.; Asmis, K. R. Structures and Vibrational Spectroscopy of Partially Reduced Gas-Phase Cerium Oxide Clusters. *Phys. Chem. Chem. Phys.* **2011**, *13* (43), 19393−19400.
(73) Pop, O. L.; Diaconeasa, Z.; Mesaroş, A.; Vodnar, D. C.; Cuibus, L.; Ciontea, L.; Socaciu, C. FT-IR Studies of Cerium Oxide Nanoparticles and Natural Zeolite Materials. *Bull. Univ. Agric. Sci. Vet. Med. Cluj-Napoca. Food Sci. Technol.* **2015**, *72* (1), 50−55.
(74) Vicario, M.; Llorca, J.; Boaro, M.; de Leitenburg, C.; Trovarelli, A. Redox Behavior of Gold Supported on Ceria and Ceria-Zirconia Based Catalysts. *J. Rare Earths* **2009**, *27* (2), 196−203.
(75) Giordano, F.; Trovarelli, A.; De Leitenburg, C.; Giona, M. A Model for the Temperature-Programmed Reduction of Low and High Surface Area Ceria. *J. Catal.* **2000**, *193* (2), 273−282.
(76) Badri, A.; Binet, C.; Saussey, J.; Lavalley, J. *In Situ FT-IR Study of Ceria Reduction by CO*. **1997**, *699*, 697−698.
(77) Berens, P. H.; Wilson, K. R. Molecular Dynamics and Spectra. I. Diatomic Rotation and Vibration. *J. Chem. Phys.* **1981**, *74* (9), 4872−4882.
(78) Basov, N. G.; Kazakevich, V. S.; Kovsh, I. B. Electron-Beam-Controlled Laser Utilizing the First Overtones of the Vibrational-Rotational Transitions in the Co Molecule - 2. Energy Characteristics. *Sov. J. Quantum Electron.* **1980**, *10* (9), 1136−1139.
(79) Mina-Camilde, N.; Manzanares, I. C.; Caballero, J. F. Molecular Constants of Carbon Monoxide at v = 0, 1, 2, and 3. *J. Chem. Educ.* **1996**, *73* (8), 804−807.
(80) Gibson, K. S. THE EFFECT OF TEMPERATURE UPON THE ABSORPTION SPECTRUM OF A SYNTHETIC RUBY. *Phys. Rev.* **1916**, *8* (1), 38−47.
(81) YEN, W. M.; SCOTT, W. C.; SCHAWLOW, A. L. Phonon-Induced Relaxation in Excited Optical States of Trivalent Praseodymium in LaF_3. *Phys. Rev.* **1964**, *136* (1A), A271−A283.
(82) Johnson, S. A.; Freie, H. G.; Schawlow, A. L.; Yen, W. M. Thermal Shifts in the Energy Levels of LaF_3:Nd^{3+}. *J. Opt. Soc. Am.* **1967**, *57* (6), 734.
(83) RICE, D. K.; DeSHAZER, G. L. Spectral Broadening of Europium Ions in Glass. *Phys. Rev.* **1969**, *186* (2), 387−392.
(84) Vilé, G.; Bridier, B.; Wichert, J.; Pérez-Ramírez, J. Ceria in Hydrogenation Catalysis: High Selectivity in the Conversion of Alkynes to Olefins. *Angew. Chemie - Int. Ed.* **2012**, *51* (34), 8620−8623.
(85) Cao, T.; You, R.; Zhang, X.; Chen, S.; Li, D.; Zhang, Z.; Huang, W. An in Situ DRIFTS Mechanistic Study of CeO_2-Catalyzed Acetylene Semihydrogenation Reaction. *Phys. Chem. Chem. Phys.* **2018**, *20* (14), 9659−9670.
(86) Carrasco, J.; Vilé, G.; Fernández-Torre, D.; Pérez, R.; Pérez-Ramírez, J.; Ganduglia-Pirovano, M. V. Molecular-Level Understanding of CeO_2 as a Catalyst for Partial Alkyne Hydrogenation. *J. Phys. Chem. C* **2014**, *118* (10), 5352−5360.
(87) Rodriguez, J. A.; Hanson, J. C.; Frenkel, A. I.; Kim, J. Y.; Pérez, M. Experimental and Theoretical Studies on the Reaction of H_2 with NiO: Role of O Vacancies and Mechanism for Oxide Reduction. *J. Am. Chem. Soc.* **2002**, *124* (2), 346−354.
(88) Lu, J.; Song, J. J.; Niu, H.; Pan, L.; Zhang, X.; Wang, L.; Zou, J. J. Periodic Density Functional Theory Study of Ethylene Hydrogenation over Co_3O_4 (1 1 1) Surface: The Critical Role of Oxygen Vacancies. *Appl. Surf. Sci.* **2016**, *371*, 61−66.
(89) Zhang, Y. C.; Pan, L.; Lu, J.; Song, J.; Li, Z.; Zhang, X.; Wang, L.; Zou, J. J. Unraveling the Facet-Dependent and Oxygen Vacancy Role for Ethylene Hydrogenation on Co_3O_4 (110) Surface: A DFT+U Study. *Appl. Surf. Sci.* **2017**, *401*, 241−247.
(90) Song, J.; Huang, Z. F.; Pan, L.; Zou, J. J.; Zhang, X.; Wang, L. Oxygen-Deficient Tungsten Oxide as Versatile and Efficient Hydrogenation Catalyst. *ACS Catal.* **2015**, *5* (11), 6594−6599.
(91) García-Melchor, M.; López, N. Homolytic Products from Heterolytic Paths in H_2 Dissociation on Metal Oxides: The Example of CeO_2. *J. Phys. Chem. C* **2014**, *118* (20), 10921−10926.
(92) Albani, D.; Capdevila-Cortada, M.; Vilé, G.; Mitchell, S.; Martin, O.; López, N.; Pérez-Ramírez, J. Semihydrogenation of Acetylene on Indium Oxide: Proposed Single-Ensemble Catalysis. *Angew. Chemie - Int. Ed.* **2017**, *56* (36), 10755−10760.
(93) Zhang, S.; Huang, Z. Q.; Ma, Y.; Gao, W.; Li, J.; Cao, F.; Li, L.; Chang, C. R.; Qu, Y. Solid Frustrated-Lewis-Pair Catalysts Constructed by Regulations on Surface Defects of Porous Nanorods of CeO_2. *Nat. Commun.* **2017**, *8* (May), 1−11.
(94) Huang, Z. Q.; Liu, L. P.; Qi, S.; Zhang, S.; Qu, Y.; Chang, C. R. Understanding All-Solid Frustrated-Lewis-Pair Sites on CeO_2 from Theoretical Perspectives. *ACS Catal.* **2018**, *8* (1), 546−554.
(95) Wang, L.; Yan, T.; Song, R.; Sun, W.; Dong, Y.; Guo, J.; Zhang, Z.; Wang, X.; Ozin, G. A. Room-Temperature Activation of H_2 by a

Surface Frustrated Lewis Pair. *Angew. Chem.* **2019**, *131* (28), 9601−9605.
(96) Christiansen, M. A.; Mpourmpakis, G.; Vlachos, D. G. Density Functional Theory-Computed Mechanisms of Ethylene and Diethyl Ether Formation from Ethanol on γ-Al_2O_3(100). *ACS Catal.* **2013**, *3* (9), 1965−1975.
(97) Lahousse, C.; Maugé, F.; Bachelier, J.; Lavalley, J. C. Acidic and Basic Properties of Titania-Alumina Mixed Oxides; Active Sites for Propan-2-Ol Dehydration. *J. Chem. Soc. Faraday Trans.* **1995**, *91* (17), 2907−2912.
(98) DeWilde, J. F.; Czopinski, C. J.; Bhan, A. Ethanol Dehydration and Dehydrogenation on γ-Al_2O_3: Mechanism of Acetaldehyde Formation. *ACS Catal.* **2014**, *4* (12), 4425−4433.
(99) Rosynek, M. P.; Koprowski, R. J.; Dellisante, G. N. The Nature of Catalytic Sites on Lanthanum and Neodymium Oxides for Dehydration/Dehydrogenation of Ethanol. *J. Catal.* **1990**, *122* (1), 80−94.
(100) Yun, D.; Herrera, J. E. A Novel Methodology for in Situ Redox Active Site Titration of TiO_2-Supported Vanadia during Ethanol Partial Oxidation Catalysis. *J. Catal.* **2017**, *350* (2), 72−85.
(101) Haffad, D.; Chambellan, A.; Lavalley, J. C. Propan-2-Ol Transformation on Simple Metal Oxides TiO_2, ZrO_2 and CeO_2. *J. Mol. Catal. A Chem.* **2001**, *168* (1−2), 153−164.

https://doi.org/10.1021/acs.jpcc.2c06637
J. Phys. Chem. C 2023, 127, 234−247